Sparse Techniques for Emission Imaging

Andrei Kharchenko[a], Julia H. Jungmann[a], Luke MacAleese[a,b], Ron M. A. Heeren[a,*]

[a]*FOM Institute AMOLF, Science Park 104, 1098 XG Amsterdam, The Netherlands*
[b]*Institut Lumière Matière, UMR5306 Université Lyon 1-CNRS, Université de Lyon 69622, Villeurbanne Cedex, France*

Abstract

Emission imaging is based on scanning an object with a photon beam or a stream of particles having high kinetic energy, amplifying the emitted particles with an intensifier device, and guiding its output secondary particles onto a position-sensitive detector which sometimes comprises a high frequency clock which provides additional separation of the sensed events in time. We show that the image is always a set of elliptical loci of secondary particles with some noise, and that the positions of the primary particles can be efficiently recognized from the intensifier's output image and all the geometric noise separated. It requires ad hoc data analysis due to the redundancy of the raw event stream which becomes under-sampled after filtering. A two-phase technique to filter geometric noise and to visualize the acquired structures addresses the redundancy and under-sampling/filtering problems. Our filtering is based on the statistical properties of particle beams which allows us to efficiently "clean" the acquired 2D images by handling all the types of inherent artifacts based on the parameters of the spatial distribution of an individual particle beam. The filtered images suffer from significant under-sampling which should be handled by some missing pixel recovery procedure, usually an interpolation. We present an overview of various interpolation approaches from 3D approximation to manifold learning, and show that the reconstruction of the corrupted spectrum sampled at the locations of beam positions produces the best image recovery.

Keywords: emission imaging, image reconstruction, Hough transform, sparse recovery, point set, simplicial complex

1. Introduction

Recent technological progress in the development of high-resolution, high-sensitivity and high-speed positional detection systems has enabled the detection of individual particle events in time and space [1] [2]. These detectors assist in the observation and registration of rapid phenomena that cannot be observed with conventional optical instruments. The development in this field is predominantly driven by high energy physics [3], astrophysics and X-ray imaging [4]. Recently, imaging mass spectrometry [5] has been added to the list of technology push factors.

---

*Corresponding author.
Email address: `rheeren@amolf.nl` (Ron M. A. Heeren)

All these applications have in common that they target an accurate positional detection of transient particle induced events. In most cases also accurate time tracing of these events is required which adds to the complexity of the required information. The application areas vary significantly in particle loads or count-rates arriving on the detector system.

Biomolecular imaging mass spectrometry [6] [7] is employed predominantly in biomedical studies where optical imaging cannot provide any detailed information without targeted labeling with fluorescently labeled antibodies or other radioactively labeled pharmaceutical or exogenous compounds. In these cases it is imperative to examine native endogenous biomolecules directly from cells or tissue sections. The operating principle is based on the desorption and ionization of intact biomolecules, immediately followed by mass spectrometric separation and structural analysis. In selected cases the spatial distribution is kept intact and direct molecular images can be acquired [8]. Biomolecular ion detection as well as UV or X-ray photon detection are based on a combination of a local conversion of the ion into one or more electrons and a subsequent amplification step on an image intensifier device, e.g. a micro-channel plate (MCP).

In this article, we present a theoretical treatment of emission imaging with the under-sampling artifact and propose an approach to retrieve maximal information from sparse imaging data sets. The approach is two-fold: First, image noise and artifacts are distinguished from the events originating from the object imaged via finding centers of elliptic envelopes of secondary event positions in a multi-dimensional parametric space. Second, the centers, insufficient for creating an image, are used for sampling the acquired image pixels' spectrum which is then reconstructed via l_0-optimization with additional criteria. A comparison with alternative methods is presented: B-spline approximation and homology learning. The presented approach is highly generic and applicable to virtually any type of sparse data set. Boundary conditions, experimental guidelines and algorithm limitations are provided to the reader. The novel method is successfully applied to benchmark data (on a resolution mask) and to "real" biomolecular imaging mass spectrometry data to demonstrate the ready applicability of the algorithms.

2. Experimental data

Two types of experimental data are used to test and illustrate the concepts developed for sparse emission imaging. Both types of experimental data are acquired with a chevron microchannel plate stack in combination with a novel type of imaging detector, an active pixel detector of the Medipix/Timepix detector family [9]. This chip consists of 256×256 pixels of 55×55 μm^2. On the single pixel level, this pixelated chip can measure (1) the number of particles impinging on the pixel, (2) the time-of-flight of a particle with respect to an external trigger, or (3) the time-over-threshold, i.e. the time interval during which the charge generated from a particle event remains above the detection threshold (i.e. a measure of particle energy). Typically, a sample is "imaged" by illumination/ablation of a specimen with a probe, e.g. photons, primary ions etc. The "image particles" are guided towards the detection system. Whenever a particle impinges on this detection system, the intensifier converts this event into an electron shower such that a one-particle-event is transformed into an electron shower of thousands to millions of electrons. This shower covers multiple pixels on the Timepix chip. Fig. 1 gives a schematic representation of the imaging setups.

The first type of experimental data, the "benchmark" data, is generated by illumination
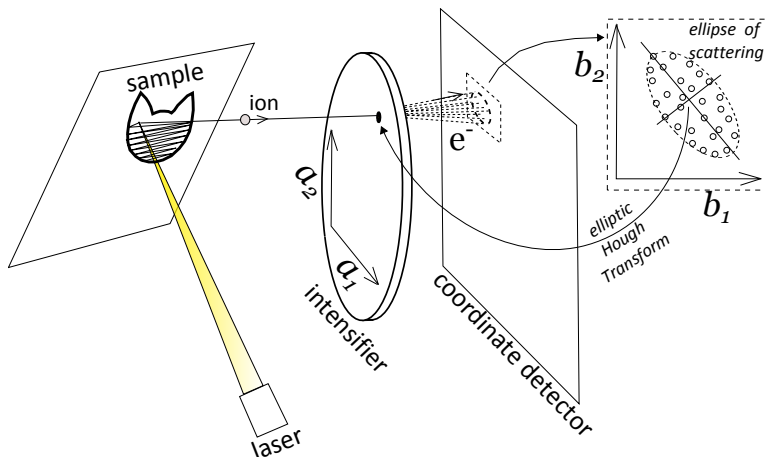

Figure 1: Principle of imaging setup: The specimen under investigation is illuminated by a particulate probe as, for instance, electrons, photons, primary ions etc. "Image particles" -secondary particles or non-absorbed photons- are guided towards the detection system. The image particles impinge on the first detector stage, the microchannel plates, which translate the event into a shower of electrons. This secondary electron shower spans multiple elements on the second detector stage, a pixelated detection system. The pixel address (x,y) provides spatial information on the particle event. Additionally, the active pixel detector provides information on, for instance, the time-of-flight of the particle (t). Successive cycles of specimen illumination result in multiple measurement frames whose information can be combined.

of a target mask with UV photons. In particular, the experimental test setup combines a 2×2 chip bare Timepix detector with a chevron-shaped stack of the intensifier channels. The distance between the intensifier MCP stack and the Timepix is about 2.5 mm. The pores of the intensifier have a diameter of 12 μm on a 15 μm centre-to-centre spacing. This detector assembly is mounted in a vacuum chamber and illuminated homogenously with photons from a 254 nm UV lamp (Pen-Ray, EW-97606-00, 4400 μW/cm^2). The lamp is mounted outside the chamber at a distance of about 20 cm from the detector assembly. The photons enter the chamber through a fused silica window and a 100 μm pinhole. A USAF 1951 resolution target (Edmund optics, Barrington, USA) was placed in direct contact with the front side of the intensifier. The resolution target pattern is deposited as a reflective chromium layer on a 1 mm thick fused silica plate ($2" \times 2"$). The resolution pattern size is about 15 mm$\times$14 mm. The line pattern corresponds to "standard resolution" meaning that minimum frequency of line pairs is found in group 0 at element 1 and that the maximum frequency of line pairs is found in group 7 at element 6. The voltages applied to the intensifier back and front side, i.e. the MCP gain and the acceleration voltage between the intensifier's back side and the Timepix detector, can be tuned in order to optimize the experimental settings for maximum spatial resolution. The presented data set is acquired in time-over-threshold mode and consists of 150,000 acquisition frames of 0.2 s each.

For the second type of experimental data, the authors choose a "real application" sample,

i. e. a data set generated by biological mass spectrometry imaging, as to demonstrate the applicability of the presented method. The sample is a nickel hexagonal thin bar transmission electron microscopy (TEM) grid (700 mesh, G2760N, 3.05 mm diameter, 37 μm pitch, 8 μm bar width; Agar Scientific Limited, Stansted, UK) placed on top of a 2 μl droplet of 1 mg/ml Peptide Calibration Standard II (Bruker GmbH, Bremen, Germany; pepmix in 50% Acetonitrile (ACN), 50% H_2O, 0.1% trifuoroacidic acid (TFA)) mixed with 10 mg/ml α-Cyano-4-hydroxycinnamic acid (HCCA in 50% ACN, 50% H_2O, 0.1% TFA) on an indium-tin-oxide (ITO) coated glass slide. The sample was measured on the AMOLF ion microscope with a MCP/Timepix detection system previously described in [5]. The Timepix chip was operated in "time-of-flight" mode, i.e. the pixels measure the time-of-flight (and hence mass-to-charge ratio) of the analyte ions with respect to the ionization laser. The data set consists of 85 data frames, each of which contains the events corresponding to a single laser shot.

3. Principle of emission imaging

The idea of imaging mass spectrometry based on a position-sensitive particle detector is simple: since the individual image intensifier channel tubes confine the primary particle pulse, the spatial pattern of electron pulses at the rear of the intensifier surface preserves the pattern of primary ion image incident on the front surface. See Fig. 1 . The common property of all such devices is that due to the Central Limit Theorem emission channels (e.g. individual intensifier channels) always produce circular or close to circular electron signal image.
Due to scattering inherent to the operation principle, the coordinate sensor input contains several types of noise:
(1) geometric – we should distinguish spurious non-circular spots and speckles from quality elliptical clusters of higher intensity;
(2) positional – variations of shape can occur, but still an ellipse;
(3) uneven intensity – usually, the internal background count, or dark noise, is uniformly distributed across the intensifier plate. The number of electrons arriving on adjacent pixels within a cluster, i.e. belonging to the same event, is not equal due to the random nature of secondary electron emission and electronic noise. See Fig. 2, 1.

4. Recovering ion positions via detecting scattering centroids

Since each primary particle is registered as a series of secondary events in a form of constant time packets, their positions can be determined up to the secondary source resolution. In turn, the secondary source's amplification cycle produces events dispersed in space and time and belonging to multiple adjacent time frames making it impossible to use just one frame to determine the dispersion envelope of a secondary shot.
A single primary event which was successfully registered by the intensifier creates a large number of secondary events. Denote J – the unknown image on the inlet of the intensifier, $I = J * H$ – the image on the outlet of the segmented coordinate detector which we can without loss of generality represent as a convolution of the undistorted image J and a point spread function H. Let $X = (X_1, X_2)$ – a random vector of Cartesian coordinates X_1 and X_2 registered with the coordinate detector, $X \subset I$. We assume that the the physical properties
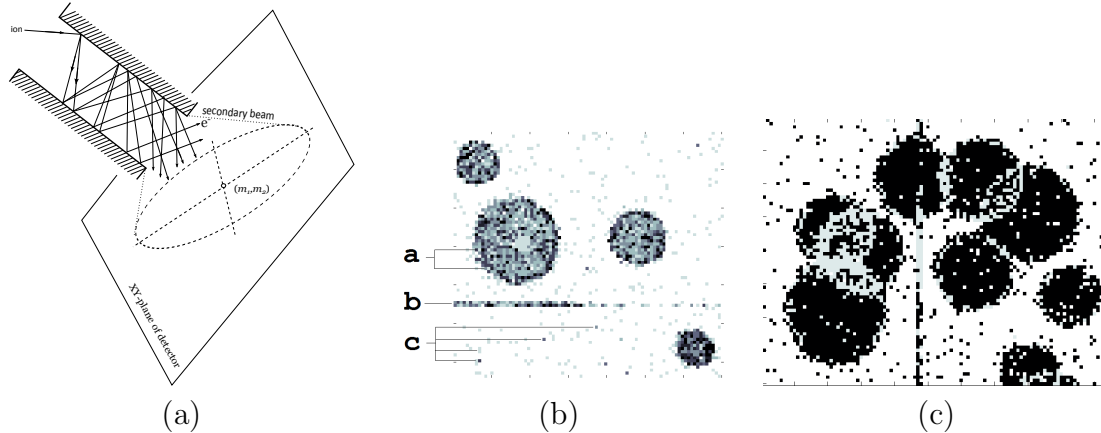
Figure 2: (a) – multiple electron reflections and scattering in the intensifier channel cause the elliptic pattern on the detector plane. (b) – types of noise in a typical emission imaging acquisition: a – irregular intensity of pixels in blob contours preventing straightforward center detection approaches e.g. center of mass from working correctly; b and c – non-elliptic shapes; c – false blobs of infinitely small radius. (c) – Centroiding challenge caused by overlapping ellipsoids.

of the segment intensifier affecting the trajectories of secondary particles do not fluctuate over time at least within amplifying a single primary particle, thus $X_{1,2}$ are generated by the same probability distribution. For any sufficiently large number n of identically distributed random values, as we know, the following (Central Limit) theorem states [20] that

$$P\left\{\frac{\sum_{i=1}^{n} X_i - mn}{\sqrt{n\sigma^2}} < l\right\} \xrightarrow[n\to\infty]{} \Phi(x) \tag{1}$$

where $\Phi(x) = \int_{-\infty}^{x} p(t, m, \sigma^2)dt$ – the cumulative function of the standard normal distribution $p(t, m, \sigma^2)$ with mean m and variance σ^2, and l – some probability, $l = $ const. The distribution function of random variable X_i, in its turn, is:

$$p_{X_i}(x) = \frac{1}{\sqrt{2\pi\sigma_i^2}}\exp\left[-\frac{(x - m_i)^2}{2\sigma_i^2}\right] \tag{2}$$

where $m_i = E(X_i)$ and $\sigma_i = D(X_i)$ are the expectation and standard deviation. Since X_1 and X_2 are independent random values, we can use the theorem

$$p_{X_1, X_2}(x_1, x_2) = p_{X_1}(x_1)p_{X_2}(x_2) \tag{3}$$

to express the joint probability density as

$$p_{X_1, X_2}(x_1, x_2) = \frac{1}{2\pi\sigma_1\sigma_2}\exp\left[-\frac{(x_1 - m_1)^2}{2\sigma_1^2} - \frac{(x_2 - m_2)^2}{2\sigma_2^2}\right]. \tag{4}$$

Due to the presence of stray electrical and magnetic fields and errors in the coordinate registration equipment caused by temperature fluctuations, registered events deviate from

the expected scattering distribution (4). Such events cannot be detected without knowledge of centers of the involved intensifier channels' distributions in the form of parameters $m_1, m_2, \sigma_1, \sigma_2$. However, they can be separated as geometric noise (Fig. 2, 1) by estimating parameters of distribution cross-sections in the corresponding space of ellipse parameters. Geometrically, $p_{X_1,X_2}(x_1, x_2)$ describes some surface in the 3-dimensional Cartesian space whose contour line in the x_1x_2-plane is $p_{X_1,X_2}(x_1, x_2) = a$ where $a = \text{const}$ – some probability. (4) can be expressed as

$$\frac{\sigma_2^2}{\sigma_1^2}(x_1 - m_1)^2 + \frac{\sigma_1^2}{\sigma_2^2}(x_2 - m_2)^2 = -\ln(2a\pi\sigma_1\sigma_2), \tag{5}$$

or

$$\frac{\sigma_2^2}{\sigma_1^2}x_1^2 + \frac{\sigma_1^2}{\sigma_2^2}x_2^2 - 2\frac{\sigma_2^2}{\sigma_1^2}x_1m_1 - 2\frac{\sigma_1^2}{\sigma_2^2}x_2m_2 = -\ln(2a\pi\sigma_1\sigma_2) - \frac{\sigma_2^2}{\sigma_1^2}m_1^2 - \frac{\sigma_1^2}{\sigma_2^2}m_2^2, \tag{6}$$

which, after denoting $c_1 = \frac{\sigma_2^2}{\sigma_1^2}$, $c_3 = \frac{\sigma_1^2}{\sigma_2^2}$, $c_4 = -\frac{\sigma_2^2}{\sigma_1^2}m_1$, $c_5 = -\frac{\sigma_1^2}{\sigma_2^2}m_2$, $c_6 = -(\ln(2a\pi\sigma_1\sigma_2) + \frac{\sigma_2^2}{\sigma_1^2}m_1^2 + \frac{\sigma_1^2}{\sigma_2^2}m_2^2)$, and $c_2 = 0$, is the conic section equation

$$c_1x_1^2 + c_2x_1x_2 + c_3x_2^2 + c_4x_1 + c_5x_2 + c_6 = 0 \tag{7}$$

which after meeting the condition $c_2^2 - 4c_1c_3 < 0$ becomes the equation of ellipse with parameter a. Technically, coordinates of the primary particles incident to the intensifier can be found by recognizing elliptical loci of secondary particles emitted by the intensifier detected with the coordinate detector. Such a recognition is done in a space of ellipse parameters, for example c_1-c_6. This will allow us to filter out the geometric noise as shapes that are non-elliptical and will be able to handle nested and overlapping elliptical event loci like in Fig. 2, 3. A popular approach for grouping points into geometric shapes is the Hough transform [15],[13] which identifies points defining shapes that can be expressed parametrically. The Hough transform maps each non-blank point separately in the image onto a curve of constant intensity in the multi-dimensional Hough space of shape parameters that represents all possible shapes through this point. If $p = (c_1^+, c_3^+, c_4^+, c_5^+, c_6^+)$ is a tuple of discretized parameters c_1, c_3, c_4, c_5, c_6 where symbol $+$ denotes discretization, for points located on the same shape, their Hough space image curves $HT(p)$ intersect in a common point $(c_1^*, c_3^*, c_4^*, c_5^*, c_6^*)$ which gives rise to a local maximum

$$(c_1^*, c_3^*, c_4^*, c_5^*, c_6^*) = \underset{c_1,c_3,c_4,c_5,c_6}{\arg\max} HT(c_1^+, c_3^+, c_4^+, c_5^+, c_6^+). \tag{8}$$

Considering the intensifier image I as the input to our scattering ellipse detection via their simultaneous parameter estimation in the Hough space, we can see that the angle $\theta =^1/_2 \arctan \frac{2\rho\sigma_1\sigma_2}{\sigma_1^2-\sigma_2^2}$ between the main ellipse axis and the x_1 axis is not necessary for estimating the ellipse center (x_0, y_0). This suggests using a simpler form of the ellipse equation than the implicit form 7 e.g.

$$\frac{(x_1 - x_{1C})^2}{d_1^2} + \frac{(x_2 - x_{2C})^2}{d_2^2} = 1 \tag{9}$$

where x_{1C} and x_{2C} are coordinates of the center that we are ultimately looking for, and d_1 and d_2 are semi-diameters, which reduces the initially planned 5-dimensional Hough space to the

4-dimensions. Second, best practices with implementing the Hough transform algorithmically suggest using binary labeled images. Accordingly, we can examine a derivative $I_g = I'$ instead of the original image I, usually obtained via the convolution $I'(x, y) = I(x, y) * K$ where K is a specific 2-dimensional convolution kernel e.g. Robert, Sobel, Prewitt, or Canny kernels [12]. Third, unlike in the original Hough transform, we only deal with complete shapes while the original Hough's approach also recognizes ellipse segments.

Let's incorporate the image gradient into an algorithm which will reduce the whole parameter locus to a line. Let $v = x_1 - x_{1C}$, $w = x_2 - x_{2C}$, then (9) becomes

$$\frac{v^2}{d_1^2} + \frac{w^2}{d_2^2} = 1 \tag{10}$$

and

$$\frac{d}{dv}\left[\frac{v^2}{d_1^2} + \frac{w^2}{d_2^2}\right] = \frac{2v}{d_1^2} + \frac{2w}{d_2^2}\frac{dw}{dv} = 0. \tag{11}$$

Remembering that $\frac{dw}{dv} = \delta$ is available via the pixel difference,

$$\frac{2v}{d_1^2} + \frac{2v}{d_2^2}\frac{dw}{dv} = 0 \Leftrightarrow v^2 = \left(\frac{d_1^2}{d_2^2}\delta\right)^2 w^2. \tag{12}$$

Now by substituting this into 10 we get:

$$\frac{w^2}{d_2^2}\left(1 + \frac{d_1^2}{d_2^2}\delta\right) = 1 \tag{13}$$

and

$$w = \pm\frac{d_2^2}{\sqrt{1 + \frac{d_1^2}{d_2^2}\delta^2}} \quad \text{and} \quad v = \pm\frac{d_1^2}{\sqrt{1 + \frac{d_2^2}{d_1^2}\delta^2}} \tag{14}$$

and then x_{1C} and x_{2C}. This somewhat complicates the solution by the need to decide upon its four possible locations by analyzing the sign of dv and dw – see algorithm 1. Finally, let V be the image of size $k \times l$ blank everywhere except at coordinates of centers produced with the algorithm 1. Every x_{1C} and x_{2C} in the algorithm output vector S is overlaid to synthesize V: $V_{x_1,x_2} = 0$ everywhere except $x_1 = \lfloor x_{1C} \rfloor$ and $x_2 = \lfloor x_{2C} \rfloor$ where $V_{x_1,x_2} = 1$. An example of applying the algorithm to real image is presented in Fig. 5, left.

5. Forming the image from scattering centroids

The output of the centroiding algorithm 1 is a set of centers having real-valued coordinates that should be resolved to intensities on a regular pixel grid from it via spatial binning as the centroid overlay image V. This image is significantly undersampled compared to its original.

The intensifier inlet image is always sparse due to the non-continuous mode of laser operation, loss of events on the coordinate detector caused by its electronic circuit, and deflection of charged particles caused by stray electric fields. Accordingly inevitable absence of gradient continuity in adjacent pixels after centroiding is usually addressed as the inpainting

Algorithm 1 Gradient elliptic Hough transform
***

Require: $I - k \times l$ sized image

Ensure: pairs (x_{1C}, x_{2C}) of enveloping ellipses' centers, pairs (d_1, d_2) of their diameters

  Temp structure: S – 4-dimensional accumulator array

  Initialize S

  for all pixel (x,y) in I **do**

    $v \leftarrow I[x+1, y] - I[x, y]$

    $w \leftarrow I[x, y+1] - I[x, y]$

    for all $d_1 \in [0, x_{max}]$ step Δ_{d_1}, $d_2 \in [0, y_{max}]$ step Δ_{d_2} **do**

      $\alpha \leftarrow arctg\left(\frac{w}{v}\right) - \frac{\pi}{2}$

      $\delta \leftarrow tg(\alpha)$

      $dx \leftarrow sign_X(v, w) \dfrac{d_1^2}{\left(1 + \frac{d_2^2}{d_1^2} \delta^2\right)^{1/2}}$

      $dy \leftarrow sign_Y(v, w) \dfrac{d_2^2}{\left(1 + \frac{d_1^2}{d_2^2} \delta^2\right)^{1/2}}$

      $x_0 \leftarrow x + \Delta_{d_1}$

      $y_0 \leftarrow y + \Delta_{d_2}$

      Update $S(x_{1C}, x_{2C}, d_1, d_2) \leftarrow S(x_{1C}, x_{2C}, d_1, d_2) + 1$

    end for

  end for

  $N_C \leftarrow 0$

  for all $S(x_{1C}, x_{2C}, d_1, d_2)$ **do**

    if $S(x_{1C}, x_{2C}, d_1, d_2) > T$ **then**

      output $S(x_{1C}, x_{2C}, d_1, d_2)$

      $N_C \leftarrow N_C + 1$
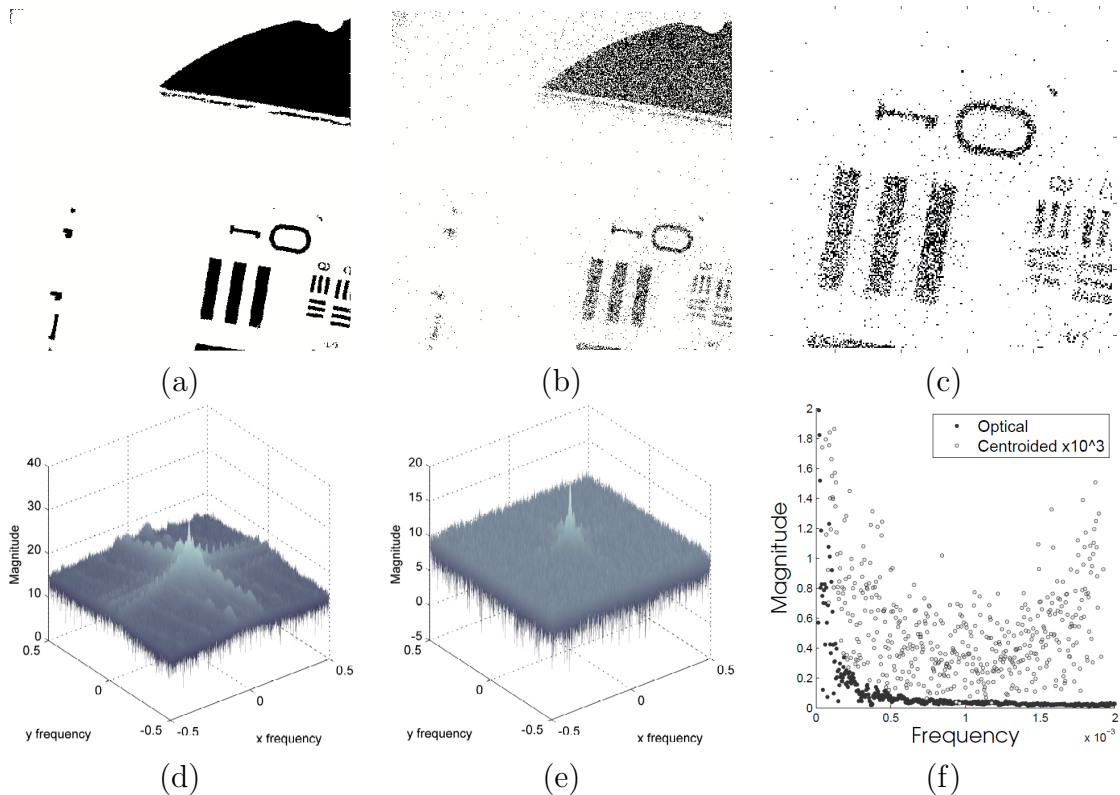
    end if

  end for
***

Figure 3: Image and 2D Fourier spectrum of an original benchmark image (a,d) and its centroid overlay (b,e). Note the sparsity of the spectrum of the original image compared to the second spectrum's density and shift in the frequency scale. (c) displays part of the resolution target as illuminated by UV photons. (f) distorted frequencies in a centroided image compared to its optical version.

problem of image analysis aimed at the recovery of missing pixels in an image, which can be implemented in a number of ways.

The simplest approach is treating the point set of known centroid coordinates $V = \{v_i\} \in R^n$ and their intensities $Z = \{z_i\} \in R$ as a 2-dimensional interpolation problem where a continuous (global) function $f : R^n \mapsto R$ can be found interpolating a given centroid image at the sample points, $f(v_i) = z_i$, and preserving higher order derivatives. This approach relies on the absence of anisotropy and on the homogeneous sampling density. In contrast, local interpolation is free of the latter shortcoming and can be implemented in a number of ways based on the knowledge of the natural neighborhood of sampled points e.g. via the Voronoi partitioning of the 2-dimensional Euclidean space (Fig. 4, a) into convex polygons $T_V = \{v \in R^n | d(v, v_i) \leqslant d(v, v_j)\}, i \neq j$, where v_i and v_j – a pair of adjacent natural neighbors and $d(\cdot, \cdot)$ – Euclidean distance on R^n. Another approach originates in the field of manifold modeling which is aimed at recognizing local topology based on sample data by connecting elements. Central to this field is the concept of simplicial complex that is a set of connected points, lines, and triangles (Fig. 4, b). Applied to the inpainting problem, the idea is to connect centroids in an intuitive way by recognizing irreducible triangles (sim-

plexes) and their connections. Such a procedure will give a representation of the point set in the form of a set of elements having a certain area. However its weakness is that it will not predict area elements beyond edge centroids.

Looking at spectra of the optical versus the centroid overlays, we observe that the spectrum
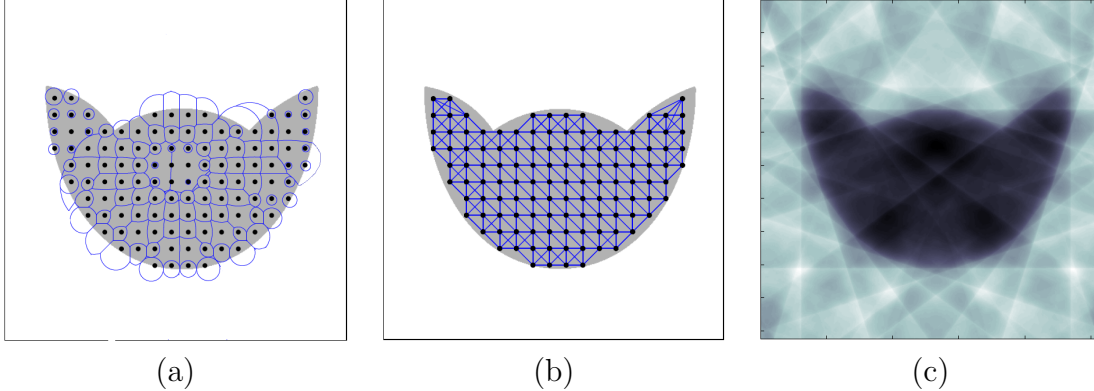

| (a) | (b) | (c) |

Figure 4: Reconstruction of an image defined by a point set with the Voronoi segmentation (a), manifold learning (b), and sparse reconstruction in the image frequency domain with 10 harmonics (c).

of the original image is rather sparse and that the overlay's spectrum is dense, distorted and forms a U-shaped pattern – Fig. 5 (f). This observation suggests another approach for the reconstruction under-sampled images – having started with the (incorrect) overlay's spectrum, iteratively adjust its spectral components to find a better representation keeping the error between the resulting inverse transform image at known centroid locations and the centroid overlay within some tight bound. This approach is motivated by the observation that the discrete Fourier spectrum of the centroid overlay is noticeably less sparse than its optical original (Fig. 5).

6. Problems with the spatial approaches

While providing with the rapidly growing signal-to-noise ratio as a function of cardinality of the sample point set, the Voronoi-based segmentation/interpolation is rather impractical computationally for real-life images due to having complexity $O(n)$ where n is the sample set cardinality [14], and $n = N_X \times N_Y$, the total number of pixels in the image. Apart from the Vietoris-Rips complex presented on 5 (c) there are other suitable simplicial complexes capable of representing an unknown manifold behind a centroid point cloud – alpha, Cech, and Smale to name a few. Unfortunately they come with even bigger computational overhead than the Voronoi segmentation. For example, constructing a Vietoris-Rips complex [19] is known to have $O(n^2)$ peak time complexity. But no matter how computationally efficient the construction of an interpolating simplicial complex is, it will fail to represent shapes without pronounced phase boundaries. On the other hand, such a difficulty is trivially represented as low frequency spectral elements in a 2D Fourier spectrum H (the third approach) whose time complexity is better: $O(n\log n)$.

(a) Imge after centroiding

(b) Spline interpolation

(c) Representation by Voronoi segmentation

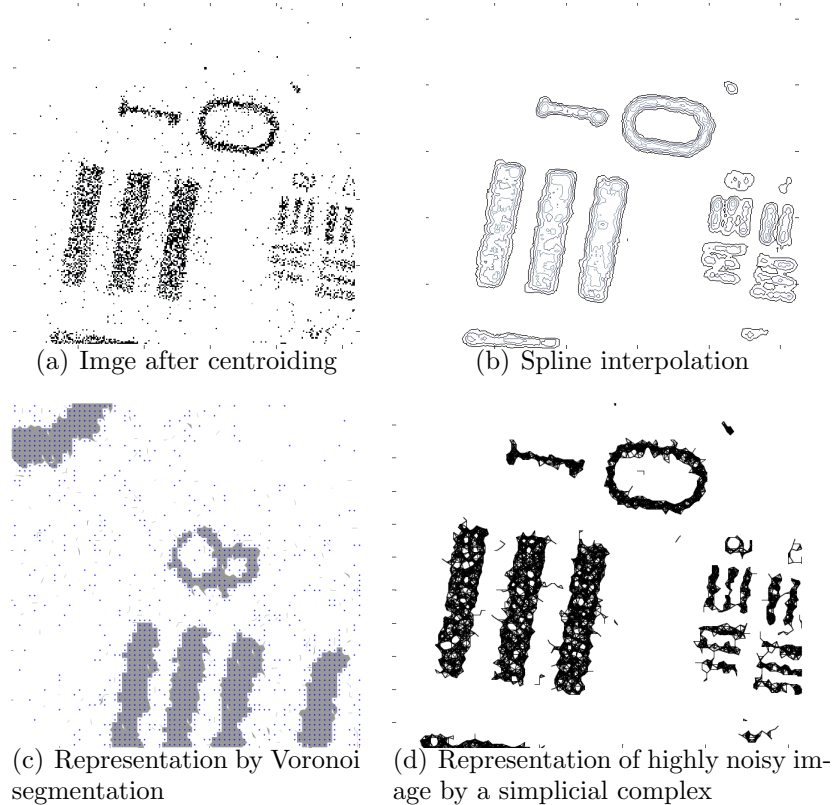(d) Representation of highly noisy image by a simplicial complex

Figure 5: Reconstruction of a highly undersampled imge with the Voronoi segmentation and manifold learning. Refer to Fig. 8 for reconstruction accuracy comparison of these methods. (a) – centroid overlay of sample size 10^3. (b) – its cubic spline reconstruction. (c) – bounded Voronoi segmentation efficiently covers co-localized informative points and filters noise. (d) – manifold learned on the undersampled image with the Vietoris-Rips-complex.

For generality, let's consider the problem in the 1-dimensional form, $\mathbf{b} = sum(A\mathbf{x})$ where A is some dictionary of directions and $\mathbf{w}$ is vector which is necessarily sparse as a result of detecting the principal directions. A needs to have the property of a uniform coverage of the direction space, and the Fourier basis is known to meet this requirement.

The spectral sparsity property is addressed by the l_0 pseudomeasure, so we can write the whole problem as:

$$\min ||\mathbf{g} - \mathbf{b}||_{l_2} \text{ subject to } \min ||\mathbf{w}||_{l_0}. \tag{15}$$

which is known to be NP-hard (very expensive computationally), but thanks to Candes, Romberg and Tao [10] we can substitute it with an almost dual convex programming problem

$$\min ||\mathbf{g} - \mathbf{b}||_{l_2} \text{ subject to } \min ||\mathbf{w}||_{l_1} \tag{16}$$

which can be successfully solved via convex optimization. Indeed, recent results [11] state that a sparse vector $\mathbf{x}_0 \in R^N$ can be recovered from a small number of linear measurements $\mathbf{b} = A\mathbf{x}_0 \in R^K$, where $K << N$. More formally, a sparse vector $\mathbf{x}_0 \in \mathbb{R}^N$ can be recovered

from a small number of linear measurements $\mathbf{b} = A\mathbf{x}_0 \in \mathbb{R}^K$ by solving a convex optimization problem

$$(P_1) : \min \|\mathbf{x}\|_1 \text{ subject to } A\mathbf{x} = \mathbf{b} \tag{17}$$

also known as basis pursuit. The Fourier spectrum of the image is small at this point but the image is not necessarily locally continuous. We can try to pursue the local continuity as a constraint to the optimization program (P_1).

Following Rudin et al. [18], the latter requirement can be implemented as minimizing the integral gradient over the entire reconstructed image. The variation norm defined as

$$D(x,y) = \left[(u_{x+1,y} - u_{x,y})^2 + (u_{x,y+1} - u_{x,y})^2 \right]^{1/2}$$

where $u_{i,j}$ – pixel value at (i,j) on the regular grid, can be used in denoising as the regularizer

$$\min_b \|\mathbf{g} - \mathbf{b}\|_{l2} + \lambda D(\mathbf{b}).$$

or form an optimization program

$$\min TV(\mathbf{x}) \text{ subject to } \|A\mathbf{x} - \mathbf{b}\|_2 \leq \varepsilon$$

where ε – tolerance, and $TV(\mathbf{x})$ – the discrete total variation of image x: $TV(\mathbf{x}) = \sum_{ij} D_{ij}\mathbf{x}$. Finally, this program can be enhanced with the sparse basis pursuit feature:

$$(P_{TV}) : \begin{cases} \min TV(\mathbf{x}) \\ \|A\mathbf{x} - \mathbf{b}\|_2 \leq \varepsilon \\ \min card(\Omega(\mathbf{x})) \end{cases}$$

where $\Omega(\mathbf{x})$ is the Fourier transform of image $\mathbf{x}$.

7. How much under-sampling is tolerable in a centroid overlay

Any practical centroid image V is undersampled and ideally we would like to have its every element available in the secondary image V^0 acquired with the coordinate detector. However, the theory of compressed sensing states that sampling the full image is wasteful in the sense that the whole signal acquired is then compressed into a small useful piece of information. Compressed sampling combines acquisition and compression into one step.

Let x^0 - n-dimensional vector of all pixels in V^0, $n = k \times l$ which we would like to reconstruct from V, and $y^0 = Ux^0$ - vector of coefficients of orthogonal transform U, $card(y^0) = n$. Vector x^0 is called S-sparse if at most S components are non-zero meaning the corresponding pixels of V^0 non-blank. x^0 can be identically recovered as $x^0 = 1/nU^*y^0$. If Ω is a sample of the transform coefficients, $card(\Omega) < card(y^0)$, then some approximation $y = U_\Omega x$ is possible, for example, in the discrete Fourier basis $y_k = \sum_{t=1}^n x(t)e^{-2i\pi(t-1)k/n} = F_\Omega x$ where $k \in \Omega$. A theorem [11] states that if

$$card(\Omega) \geqslant CS \log n \tag{18}$$

then the recovery is exact with overwhelming probability controlled by the probability of success C. We see that factors behind the accuracy of sparse reconstruction are the constant
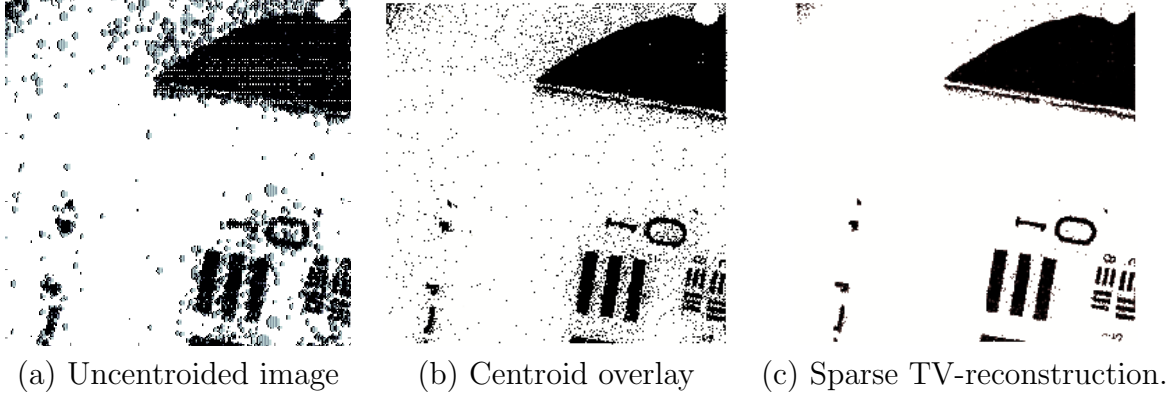
(a) Uncentroided image   (b) Centroid overlay   (c) Sparse TV-reconstruction.

Figure 6: A sparse l_1-minimization spectral reconstruction with the TV-regularization (c) applied to a noisy overlay of 10^4 centroiding samples (b) versus the raw (uncentroided) coordinate sensor input image.

C and the specific way that elements of y^0 are indexed by Ω. Tuning these factors as well as their correlation with parameters of spatial techniques (Voronoi segmentation and manifold representation) is the subject of work in progress.

In this paper, we showcase our image reconstruction techniques on deconvolving microscope mode MS images generated with the novel Timepix detector. Fig. 7 presents an application of this approach to a practical imaging mass spectrometry task. In this MSI experiment, a TEM grid on top of a peptide solution is imaged (as described in section 2). The image displays the peptide signal from underneath the honeycomb metal grid. Fig. 7a displays the raw MSI image (centroided?!), i. e., the intensity of the total ion current originating from 85 laser shots on one position on the sample surface is displayed. Fig. 7b shows the same data set after reconstruction with a three-dimensional cubic spline. For comparison, Fig. 7c displays the total variation reconstruction of the same data set. As apparent from Fig. 7, the centroided image is rather sparse such that incomplete analytical information is displayed. After reconstruction with either the 3D cubic spline or the total variation method, the full analytical information becomes available.

Fig. 8 compares the performance of the presented reconstruction approaches, i. e., it compares the signal-to-noise ratio (SNR) of the images reconstructed by the bounded Voronoi (blue), the xxx (red) and the sparse total variation reconstruction, respectively. This figure reveals that manifold segmentation techniques, like the natural neighborhood segmentation method or manifold modeling via a simplicial complex, are most suitable for very sparse, undersampled images. These techniques have a pronounced phase separation but fail to utilize the directional information contained in the data set. Contrarily, techniques based on sparse spectral representations can both address the directional information of the data set and represent halftones better. These techniques are more suitable for more dense images. Finding the exact duality between manifold modeling and sparse spectral representations and combining them is a topic of our ongoing work. Practically, and particularly interesting to mass spectrometry imaging and other sampling techniques, the presented analytical approach can determine the optimum, least-time consuming experimental approach. For instance, this
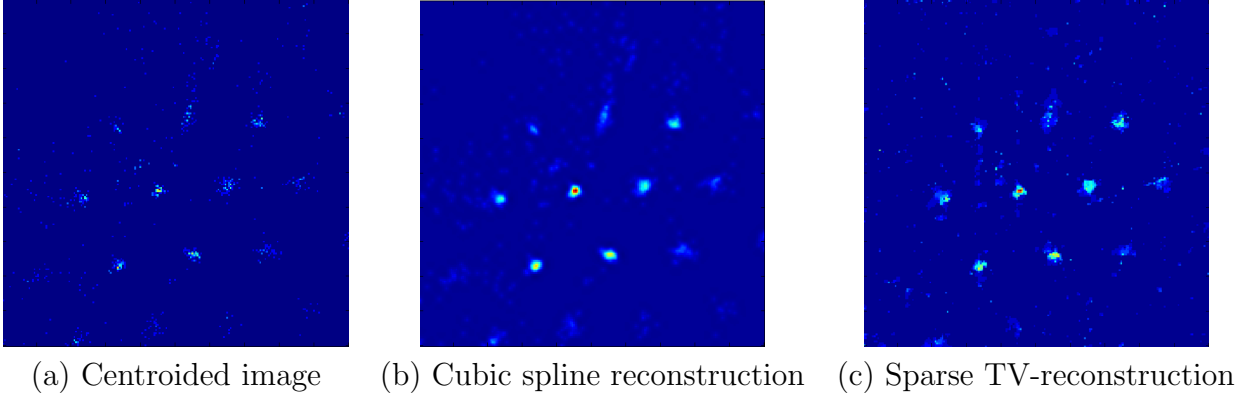
(a) Centroided image   (b) Cubic spline reconstruction   (c) Sparse TV-reconstruction

Figure 7: The mass spectrometry image of a TEM gird is displayed as an example of the reconstruction of a real biomolecular imaging acquisition. The data is treated by centroiding binned on the 512×512 grid (left), by reconstruction with a 3-dimensional cubic spline (center), by total variation reconstruction (right).

method can predict (on the basis of an optical image of the sample under investigation) the number of image frames that need to be acquired to obtain an analytically complete image!
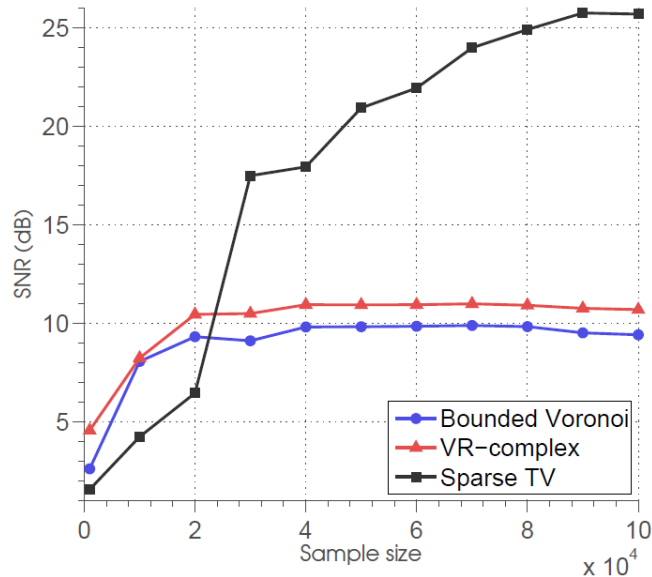

Figure 8: Performance of the reconstruction approaches.

8. Conclusion

Based on recent advances in detector instrumentation, emission imaging techniques can produce datasets of high-precision positional information with the extra time dimension.

Imaging temporal phenomena particularly is particularly useful to the imaging mass spectrometry community. Mass spectrometry imaging exposes a sample with an energy source (e. g. emitting primary charged particles), guiding them through an intensifier which creates a beam of registrable secondary particles which are detected with the positional sensor.

However, the sensor's high precision is only available after surmounting a number of image processing challenges caused by scattering inherent to emission imaging like interpreting detector events as credible shapes, filtering out geometric noise, and producing human-readable images from extremely under-sampled point sets. We observed that sensor images consist of ellipsoidal loci of time-resolved events sharing specific geometric properties due to the statistical nature of scattering of large amounts of particles. We propose to translate those loci back to coordinates of corresponding primary events via detecting elliptical loci in the parametric space via the ad hoc Hough transform thus efficiently addressing the first two challenges in one step.

The resulting point set is a high-resolution sample of the original image with a significant degree of sparseness whose missing pixels can be recovered with the interpolation. Several techniques can be applied to solve this problem and reveal the optimum amount of information from a sparse emission data set. In this work, we demonstrate that manifold segmentation techniques are most suitable for sparse, undersampled images , while techniques based on sparse spectral representations can also address directional information and represent halftones which makes them suitable to more dense images.

Mass spectrometry imaging and generally sampling techniques can benefit from the presented analytical methods to optimize the experimental sampling. The presented method can predict the least-time consuming experimental approach by analyzing how many sparse, experimental data frames are required for an analytically complete set of information. This can significantly reduce the measurement time, which is beneficial to the analysis of biologically degrading samples or clinical applications. In addition, the spatial blurring introduced by the nature of emission imaging is reduced by the presented reconstruction methods. The presented methods and mathematical algorithms reveal the full information contained in sparse emission images/data sets, which makes these methods a powerful tool that is of interest to the mass spectrometry imaging community as well as the users of other sampling techniques.

9. Acknowledgements

References

[1] M. Campbell, 10 years of the Medipix2 Collaboration, Nucl. Instrum. Meth. A, 633, Supplement 1, S1-S10, 2011

[2] J. H. Jungmann, R. M. A. Heeren. Detection Systems for Mass Spectrometry Imaging -A Perspective on Novel Developments with a Focus on Active Pixel Detectors. Rapid Commun. Mass Spectrom., accepted for publication, 2013

[3] M. H. Campbell, E. H. M. Heijne, G. Meddeler, E. Pernigotti, W. Snoeys. A readout chip for a 64×64 pixel matrix with 15-bit single photon counting. IEEE Trans Nuc Sci., 45, 751-3, 1998

[4] N. Boudet, J. F. Berar, L. Blanquart, P. Breugon, B. Caillot, J. C. Clemens, et al. XPAD: a hybrid pixel detector for X-ray diffraction and diffusion. Nucl. Instrum. Meth. A, 510, 41-4, 2003

[5] J. H. Jungmann, L. MacAleese, J. Visser, M. J. J. Vrakking, R. M. A. Heeren. High Dynamic Range Bio-Molecular Ion Microscopy with the Timepix Detector. Anal. Chem., 83, 7888-94, 2010

[6] L. A. McDonnell, R. M. A. Heeren. Mass spectrometry imaging. Mass Spectrom Rev., 26, 606-43, 2007

[7] K. Chughtai, R. M. A. Heeren. Mass Spectrometric Imaging for Biomedical Tissue Analysis. Chemical Reviews, 110, 3237-77, 2010.

[8] S. L. M. Luxembourg, T.H. Mize, L. A. McDonnell, R. M. A. Heeren. High-Spatial Resolution Mass Spectrometric Imaging of Peptide and Protein Distributions on a Surface. Anal Chem., 76, 5339-44, 2004.

[9] X. Llopart, R. Ballabriga, M. Campbell, L. Tlustos, W. Wong. Timepix, a 65k programmable pixel readout chip for arrival time, energy and/or photon counting measurements. Nucl. Instrum. Meth. A, 581, 485-494, 2007

[10] E. J. Candes, J. Romberg and T. Tao. Stable signal recovery from incomplete and inaccurate measurements. Comm. Pure Appl. Math., 59, 1207-1223, 2006

[11] E. J. Candes, J. Romberg and T. Tao. Robust uncertainty principles: exact signal reconstruction from highly incomplete frequency information. IEEE Trans. Inf. Theory, 52, 489-509, 2006

[12] L. S. Davis. A survey of edge detection techniques. Computer Graphics and Image Processing. 4, 3, 248-260, 1975

[13] R. O. Duda and P. E. Hart. Use of Hough transform to detect lines and curves in pictures. Communs Ass. comput. Mach. 15, 11-15, 1975

[14] M. Golin, H.S. Na. On the average complexity of 3D-Voronoi diagrams of random points on convex polytopes. Computational Geometry, 25, 3, 197-231, 2003

[15] P. V. C. Hough. Method and means for recognizing complex patterns. U.S. Patent 3069654, 1962

[16] S. S. Chen, D. L. Donoho, and M. A. Saunders. Atomic decomposition by basis pursuit. SIAM J. Sci. Comput., 20, 1, 33-61, 1998

[17] M. Rudelson and R. Vershynin. On sparse reconstruction from Fourier and Gaussian measurements. Communications on Pure and Applied Mathematics, 61, 8, 1025-1045, 2008

[18] L. I. Rudin, S. Osher, E. Fatemi. Nonlinear total variation based noise removal algorithms. Physica D, 60, 259-268, 1992

[19] A. Zamorodian. Fast construction of the Vietoris-Rips complex. Computers & Graphics, 34, 3, 263-271, 2010

[20] S. S. Wilks. Mathematical Statistics. John Wiley & Sons Inc, 644, 1962